Sustainable Environment Research

RESEARCH Open Access

# Towards biowastes valorization: Peanut shell as resource for quality chemicals and activated biochar production

Carla S. Fermanelli[1*], Adrián Chiappori[2], Liliana B. Pierella[3] and Clara Saux[2]

## Abstract

The purpose of this work was to transform a regional biowaste into value-added chemicals and products through a modest thermo-catalytic pyrolysis process. ZSM-11 (Zeolite Socony Mobile-11) zeolites modified by nickel (Ni) incorporation (1–8 wt%) were synthesized and characterized by means of X-Ray Diffraction, Inductively Coupled Plasma Atomic Emission Spectroscopy, Infrared Fourier Transform Spectroscopy, UV–Vis Diffuse Reflectance Spectra and Temperature Programmed Reduction. Results demonstrated that Ni was mainly incorporated as oxide. These porous materials were evaluated as heterogeneous catalysts to improve biooil composition. In this sense, higher hydrocarbon yields, and quality chemicals were obtained and oxygenates were diminished. The deactivation of the most active material was studied over six cycles of reaction. In order to achieve the circular bioeconomy postulates, the obtained biochar (usually considered a residue) was further transformed through a physicochemical activation. The obtained activated biochars were extensively characterized.

**Keywords:** Biomass pyrolysis, Biooil upgrade, Ni-ZSM-11, Activated biochar, Zero-waste approach

## 1 Introduction

In its 17 Sustainable Development Goals, the United Nations promotes the principle of optimum and responsible usage of resources for purposes leading to a convincing transition to a circular economy. The main idea of the so-called circular economy consists in advanced redesigning and technological breakthroughs to minimize waste [1]. From these ideas, the concept of "circular bioeconomy" is proposed to be a more efficient biobased renewable resource management. This term integrates the circular economy principles with the bioeconomy theory [2].

Biomass is a promising alternative to fossil resources because of its carbon richness. But considering its importance for food production, a competitive situation should be avoided. In this sense, agricultural wastes are ideal candidates for fuels and chemicals production. Peanut is an important grain legume cultivated worldwide with a growing trend of production of about 48 Mt [3]. Argentina is the 8th world peanut producer, with around 1.3 Mt produced in 2019/2020 campaign. In view of these high quantities, it is important to consider the wastes that peanut processing generates. A 25 wt% of the production corresponds to the shell, a by-product not properly used. Keeping in mind the concept of circular economy, peanut shell (PS) could be considered as the feed of an integral process.

PS contains around 50% cellulose, 20% hemicellulose and 30% lignin [4] that makes it difficult to digest and unable as feedstock for animals. Furthermore, biodegradation is extremely low, resulting in the need of severe treatments to process this kind of material. Hence, fast pyrolysis seems to be a good alternative in order to treat and give value to this biowaste. In a previous paper [5] we have shown the importance of this thermal process.

* Correspondence: cfermanelli@frc.utn.edu.ar
[1]Phytophalogy and Agricultural Modeling Unit, National Institute of Agricultural Technology, 5020 Cordoba, Argentina
Full list of author information is available at the end of the article

As proposed by Dai et al. [6], the use of zeolites as catalysts in pyrolysis reactions could improve hydrocarbons and aromatics yields. Particularly, they have found that nickel (Ni) modified zeolites promoted pyrolysis vapor deoxygenation and selectivity to aromatic compounds. The use of Ni promoted catalysts in biomass pyrolysis has been studied by many researchers. Most studies focused on ZSM-5, Mobil Composition of Matter or different oxides [7], but the use of Ni modified ZSM-11 (Zeolite Socony Mobile-11) zeolite has hardly been investigated.

As in any production system, biomass fast pyrolysis also generates waste. The solid product of pyrolysis, commonly known as biochar is usually disposed of and not further utilized. Taking Olofsson and Borjesson [8] ideas, and in order to minimize residues generation, we propose a case of open-loop recycling by employing the biochar in a subsequent system: synthesis of activated biochar (AB). This porous material can be used in Li-ion batteries, gas-phase adsorption or as heterogeneous catalysis. AB has shown great attention from the scientific community since its extraordinary properties, sustainability and low cost of production, when biowastes are employed as sources [9]. The unique physicochemical characteristics of AB should be an ideal candidate for environmental remediation purposes. Large surface area, meso and macropores system and reactive surface chemistry are the required conditions for good adsorbent performance.

The purpose of this study is to propose a two-step process for PS, which is a regionally generated biowaste. In the first step, PS is transformed into platform chemicals. In the second step, residues are transformed into AB (Fig. 1). This innovative approach is better than existing approach since it promotes near-zero-waste conditions by recycling an agricultural biowaste in two subsequent product systems.

Considering the starting biomass composition, a thermo-catalytic pyrolysis method is proposed. In order to obtain higher hydrocarbons and aromatics yields in the biooil, the effect of Ni-ZSM-11 catalyst is evaluated.

## 2 Experimental section

### 2.1 Biomass

PS was provided by the company Lorenzati, Ruetsch y Cia., from Córdoba, Argentina. The following pretreatments were applied to PS: (1) washing to remove soil particles, (2) drying at 105 °C until constant weight, (3) grinding and (4) screening to obtain a PS particle size < 3.35 mm (ASTM E 11/95). Detailed characterization of biomass has been presented in a previous work [5].

### 2.2 Catalysts synthesis and characterization

The microporous Na-ZSM-11 zeolite (Si/Al = 23) was prepared by hydrothermal synthesis [10]. Ni-zeolites were prepared by the wet impregnation method. Three concentrations of nickel aqueous solutions ($NiCl_2 \cdot 6H_2O$, Cicarelli) were used to reach a Ni-content of 1, 5 and 8 wt%. The zeolite was dispersed in the Ni solution at room temperature. Afterwards, the solvent (water) was slowly removed by rotary vacuum evaporation at 80 °C until complete dryness. Finally, the samples were dried at 110 °C overnight and subjected to a thermal treatment consisting of desorption in $N_2$ and calcination in air at 500 °C for 8 h. The as-prepared catalysts were named Ni (1) Z, Ni (5) Z and Ni (8) Z, according to metal concentration.

Nickel content was determined by inductively coupled plasma (ICP) atomic emission spectroscopy with an OPTIMA Perkin Elmer equipment. The crystalline structure of the catalysts was determined by means of X-ray diffraction (XRD) employing an X'pert PANalytical diffractometer with CuKα radiation (1.54 Å). The data were

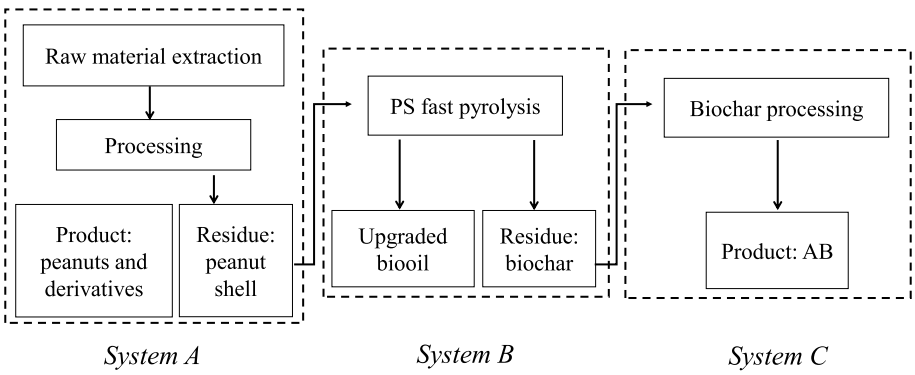


**Fig. 1** Schematic illustration of open-loop recycling between three systems. "Adapted from Journal of Cleaner Production, Vol 196, Johanna Olofsson and Pal Borjesson, Residual biomass as resource – Life-cycle environmental impact of wastes in circular resource systems, 997-1006, Copyright (2018), with permission from Elsevier"

collected in 2θ range of 5–60° in steps of 0.026° with a count time of 2 s at each point.

Surface area determinations ($S_{BET}$) using Brunauer–Emmett–Teller (BET) method were carried out with $N_2$ absorption at 77 K in a Pulse Chemisorb equipment Micromeritics 2700. The $S_{BET}$ was determined for fresh and spent catalysts (after the reaction).

Temperature programmed reduction (TPR) studies were done over Ni-zeolites in a Pulse Chemisorb 2720 equipment from Micromeritics. UV–Vis diffuse reflectance spectra (UV–Vis DRS) in absorbance mode were recorded using a Jasco V 650 spectrometer in the wavelength range 200 to 900 nm.

Infrared Fourier Transform Spectroscopy (FTIR) studies were done to determine acidity of catalysts, employing a Thermo Nicolet iS10. Pyridine was first adsorbed to the materials at room temperature under vacuum conditions and was further desorbed at 250 °C and 0.133 Pa. Acids sites quantification was done from the bands of 1545 $cm^{-1}$ (Brønsted) and 1450 $cm^{-1}$ (Lewis) using the literature data of the integrated molar extinction coefficients [11].

The amount of coke deposited on the spent catalysts was measured by thermogravimetric analysis (TGA) using a Mettler Toledo thermobalance (TGA/SDTA851e/SF/1100 °C). The sample was heated from 25 to 900 °C at a heating rate of 10 °C $min^{-1}$ under 75 mL $min^{-1}$ of air flow. Equation (1) was used to calculate the relative amount of coke [12].

$$Y_{coke}\,(wt\%) = \frac{m_{100°C} - m_{900°C}}{m_{900°C}}\,100 \tag{1}$$

where $m_{100\,^\circ C}$ and $m_{900\,^\circ C}$ correspond to the catalyst mass at 100 and 900 °C, respectively.

Functional structure of spent catalysts was characterized by XRD and FTIR using the equipment depicted above. In the case of FTIR, the KBr technique was employed.

### 2.3 Pyrolysis reactions

PS pyrolysis and biooil upgrade were simultaneously carried out in a fixed bed glass reactor (23 mm i.d., 290 mm length) under $N_2$ flow (60 mL $min^{-1}$). For a typical experiment, PS (1 g) was loaded in a glass sample carrier over a catalytic bed. The bed consisted of catalyst (1 g) and milled quartz (7 g). The reactor was introduced in an electric furnace once the pyrolysis temperature (500 °C) was reached. Condensable vapors were collected at the reactor output in a condenser (<– 10 °C). The reactions lasted 10 min. Three repeats of every experimental run were done. Average values are reported.

Equations (2), (3) and (4) were used to calculate products yields.

$$Y_{biochar}\,(wt\%) = \frac{M_{biochar}}{M_o}\,100 \tag{2}$$

$$Y_{biooil}\,(wt\%) = \frac{M_{bio-oil}}{M_o}\,100 \tag{3}$$

$$Y_{gas}\,(wt\%) = 100 - [Y_{biooil} + Y_{biochar} + Y_{coke}] \tag{4}$$

where, $M_o$ is the initial mass of the biomass sample (g), $M_{biochar}$ is the mass of the solid product (g) after the reaction and $M_{biooil}$ is the mass of the liquid product (g).

Catalyst stability was assessed by using one catalyst sample for six consecutive reaction cycles. Every new reaction was carried out employing the catalyst from the preceding cycle (i.e., the partially deactivated catalyst) maintaining the 1:1 biomass to catalyst mass ratio. Biooil was collected and analyzed after each reaction cycle.

### 2.4 Products analysis and characterization

Chemical composition of biooil was assessed by the GC-MS technique in a Perkin Elmer Claurus 600 GC coupled with an ion trap MS in a full scale mode (*m/z* 40 to 550). An Elite 5MS capillary column (30 m length, 0.25 mm i.d.) was employed and He was used as carrier gas. Chromatographic peaks were identified by means of NIST MS library and the use of standards such as acetic acid, methanol, toluene, xylenes, furfural, and 5-hydroxymethyl furfural (5-HMF). Peak area calibration was accomplished through specific response factors for each chemical group. The selectivity to each compound was calculated using Eq. (5):

$$S_i(wt\%) = \frac{A_i\,R_i}{\sum_{i=1}^{n} A_i\,R_i}\,100 \tag{5}$$

where $A_i$ is the absolute peak area of compound $i$ and $R_i$ is the response factor of compound $i$.

### 2.5 Activated biochar synthesis and characterization

AB synthesis was carried out following the protocol published by Fu et al. [13], due to its simplicity and effectiveness. A mechanical mixture of KOH (Strem Chemicals, 85%) and biochar was made in the proportions of 1:1 and 3:1 by weight. The mixture was placed in a fixed bed reactor and submitted to thermal treatment under $N_2$ atmosphere (20 mL $min^{-1}$). The heating rate was 20 °C $min^{-1}$ until 750 °C, maintaining that temperature for 3 h. The as-prepared materials, named AB 1:1 and AB 3:1, were then neutralized and washed with distilled water until pH = 7 and dried in an oven at 120 °C until constant weight.

AB yields were calculated employing Eq. (6), where $M_{biochar}$ corresponds to the mass of the biochar (g) after the pyrolysis reaction, $M_{AB}$ is the mass of the as-

prepared activated biochar (g) after the synthesis procedure.

$$Y_{AB}\ (wt\%) = \frac{M_{AB}}{M_{biochar}}\ 100 \quad (6)$$

The crystalline structure, FTIR spectra and $S_{BET}$ of AB were determined in the equipment depicted above. For FTIR analysis, the samples were prepared by blending a few milligrams of the AB sample with KBr.

Morphological analyses were done by Scanning Electron Microscopy (SEM) employing a microscope FE-SEM Σigma. It was operated at an acceleration voltage of 5 kV. Prior to analysis, the samples were coated with gold. Proximate analysis of AB was also performed using the thermobalance depicted above and following Saldarriaga et al. [14] protocol.

A LabRam spectrometer (Horiba-Jobin-Yvon) coupled to an Olympus confocal microscope was used to obtain the Raman spectra of AB samples. The spectrometer was equipped with a CCD detector at ~ 200 K, the excitation wavelength was 532 nm and the laser power was set at 30 mW.

## 3 Results and discussion

### 3.1 Catalyst characterization

The physicochemical properties of the catalysts are shown in Table 1. It can be seen that surface area of fresh materials varied as a function of Ni content. In general, when metal is loaded on porous supports, the surface area decreases due to the pore blockage and metal sintering during the calcination step [15]. $S_{BET}$ for spent catalysts showed a 23–35% decrease, compared to the fresh samples. It was observed that the reduction in $S_{BET}$ was larger when the initial $S_{BET}$ was higher.

The ICP analysis of the materials confirmed the theoretical Ni quantities, which agreed with the experimental results.

The FTIR spectra of the Ni-zeolites samples desorbed at 250 °C are shown in Fig. 2A. Bands at ~ 1450, 1492 and 1545 $cm^{-1}$ can be observed. The band at 1545 $cm^{-1}$ corresponds to the Brønsted Acid Sites (BAS) formed by the framework Al species through the Si–OH–Al bridge. This band is ascribed to the interaction of pyridinium ion binding on BAS. The band at ~ 1450 $cm^{-1}$ is related to the Lewis Acid Sites (LAS) formed by the extra framework Al species and electronic defaults in the framework aluminum [16]. The band at 1492 $cm^{-1}$ corresponds to the vibration of pyridine adsorbed over both LAS and BAS [17].

From Table 1 and Fig. 2A it can be seen that the total amount of LAS increased dramatically when the Ni was incorporated to the pristine zeolites. It is well known that the addition of Ni to zeolites modifies the acidic properties of the material [18]. The metal can create new LAS associated with $Ni^{2+}$ and NiO. The highest LAS amount was observed in the sample Ni (5) Z, in accordance to the literature, for similar zeolites [19]. After Ni incorporation, BAS slightly decreased in the case of the Ni (1) Z sample, but were significantly augmented in the case of the Ni (5) Z catalyst. On further increase of the metal content to 8 wt%, a reduction in both LAS and BAS quantification was observed. This phenomenon could be a consequence of the inaccessibility of pyridine to some of these sites as a result of the pore blockage caused by the larger oxide particles. In any case, the total amount of acid sites increased in all modified samples compared with the parent zeolite.

The XRD patterns of the catalytic materials presented in Fig. 2B confirmed the ZSM-11 structure for all the zeolites. In this way, it was possible to observe the characteristic signals at 2θ of 7–9° and 23–24° [20]. The diffraction pattern of NiO was also incorporated in this figure and the presence of its characteristic signals was emphasized (37 and 44°). The intensity of these peaks increased when the amount of the metal incorporated augmented.

Results of reducibility of Ni species are presented in Fig. 2C. All samples presented similar profiles, consisting mainly of a peak centered around 350–400 °C, while Ni (8) Z exhibited another broad peak at around 550 °C. The intensity and peak area of the Ni-zeolites spectra increased with Ni contents. The peak centered at lower temperatures corresponds to the highly dispersed Ni species, which have weak interactions with the support [21]. This peak can be attributed to the reduction of NiO to metallic nickel. It is noticeable that at higher metal content the signal became wider as consequence

**Table 1** Physicochemical and textural characteristics of the catalysts

| Catalyst | Ni[a] (wt%) | $S_{BET}$ ($m^2\ g^{-1}$) | | Lewis (μmol Py $mg^{-1}$) | Brønsted (μmol Py $mg^{-1}$) | Total acidity (μmol Py $mg^{-1}$) |
|---|---|---|---|---|---|---|
| | | Fresh | Spent | | | |
| HZ | 0.00 | 378 | 249 | 8 | 69 | 77 |
| Ni(1)Z | 0.76 | 331 | 260 | 49 | 62 | 111 |
| Ni(5)Z | 5.40 | 321 | 221 | 98 | 124 | 222 |
| Ni(8)Z | 7.40 | 287 | 221 | 53 | 55 | 108 |

[a] Determined by ICP

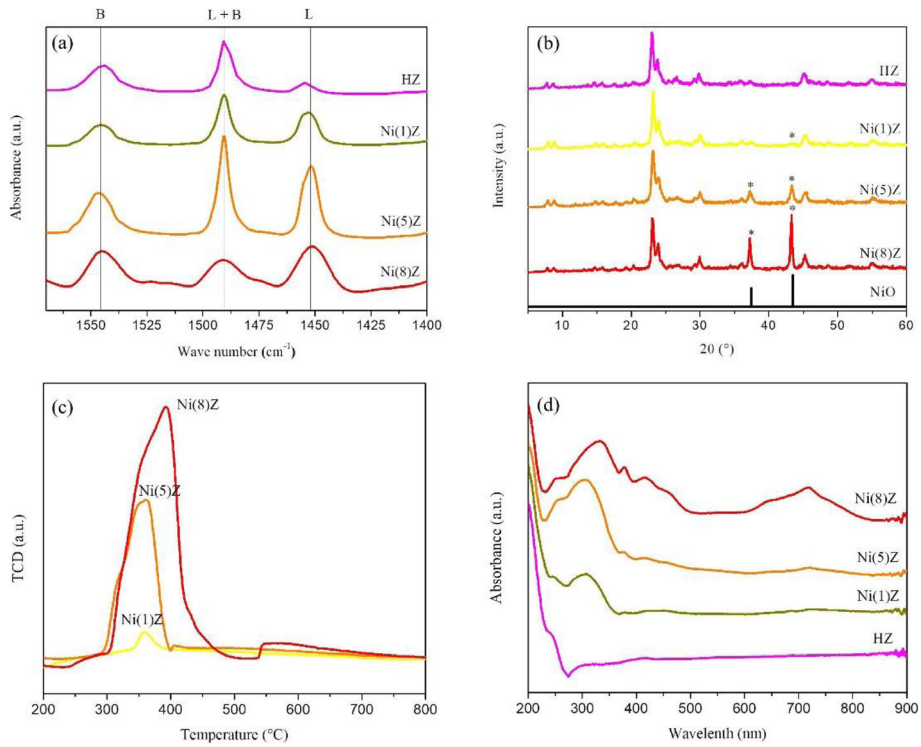


**Fig. 2** (**A**) FTIR spectra (L: Lewis; B: Brønsted) (**B**) XRD patterns, (**C**) TPR profiles and (**D**) UV-Vis DR spectra of Ni-zeolites

of diffusional limitations for bigger oxide particles. The second peak, centered at higher temperatures, can be assigned to Ni species with stronger interaction with the zeolite surface [19]. It is possible to infer that these species are also present in Ni (5) Z, but they are more prominent at higher metal content.

Figure 2D presents DRS UV–Vis spectra of the samples in order to verify the chemical environment of Ni present on them. As observed, the HZ spectrum presents a band at 200 nm that could be assigned to Al–O charge-transfer transition of four–coordinated framework Al, while the shoulder at 250 nm has been assigned to highly ordered structures with octahedral symmetry [22]. All Ni modified samples present the characteristic band of NiO around 320 nm. In the case of Ni (8) Z there is a shift in this band to higher wavelength that may correspond to higher oxide particles [23], in accordance with XRD and TPR results. This observation confirmed the previous analysis made for the acid sites of the materials. Ni (8) Z, as consequence of the higher metal content presents the larger oxide particles that block some pores. Thus, internal acid sites became inaccessible. For this sample, bands at 390, 429 and 725 nm, characteristic of NiO, became more evident and their intensity increased as Ni content was higher.

Even when NiO is predominant in all the Ni-samples, there are also some absorption bands assigned to $Ni^{2+}$ octahedrally coordinated (410, 650 and 740 nm) [24] indicating the coexistence of both species.

### 3.2 Catalytic activity

In order to determine Ni loading effect in ZSM-11 catalytic activity for biomass pyrolysis, a series of experiments were performed. Table 2 presents the mass balance of PS pyrolysis reactions catalyzed by the studied materials. As can be observed, biooil yields were similar in Ni (5) Z and Ni (8) Z catalyzed reactions. Nevertheless, a slight reduction in the biooil yield was verified when HZ and Ni (1) Z zeolites were employed. This result is a consequence of the increased selectivity towards permanent gases that occurs during the cracking of longer chain molecules.

With respect to biochar yield, it ranged around 29–30 wt%. These small variations were mainly caused by experimental error and the natural heterogeneity of PS.

**Table 2** Mass balance of PS pyrolysis reactions catalyzed with Ni-zeolites

| | Biooil (wt%) | Biochar (wt%) | Gas (wt%) | Coke (wt%) |
|---|---|---|---|---|
| Thermal | 50.8 ± 2.5 | 28.6 ± 1.4 | 20.7 ± 1.0 | |
| HZ | 47.8 ± 2.4 | 27.5 ± 1.4 | 17.4 ± 0.9 | 7.2 ± 0.4 |
| Ni(1)Z | 44.8 ± 2.2 | 29.3 ± 1.5 | 21.2 ± 1.1 | 4.7 ± 0.2 |
| Ni(5)Z | 50.0 ± 2.5 | 30.3 ± 1.5 | 15.3 ± 0.8 | 4.4 ± 0.2 |
| Ni(8)Z | 50.4 ± 2.5 | 28.9 ± 1.5 | 14.8 ± 0.7 | 5.9 ± 0.3 |

Considering the experimental set up, only pyrolysis vapors pass through the catalytic bed, so this observation could not be ascribed to a catalytic effect.

When analyzing coke yields, it was observed that the parent zeolite registered the highest coke deposition among the studied materials, suggesting that Ni incorporation to ZSM-11 zeolites prevents the formation of these carbonaceous products. This result is in agreement with Stanton et al. [25] who found that Ni-modified ZSM-5 zeolites generated lower coke deposits, compared with the unmodified fresh ZSM-5 catalyst. It is well known that coke deposits over catalysts can be generated by (1) polymerization of phenolic compounds (called thermal origin) and (2) transformation of oxygenated compounds over catalyst acid sites (called catalytic origin). Catalysts properties like porosity, particle size and surface area play an important role in coke formation [26].

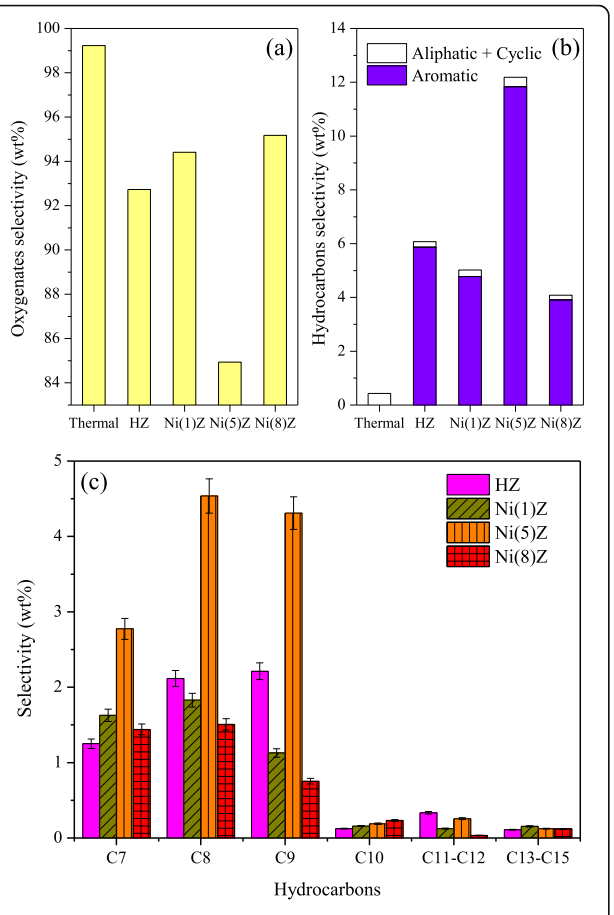


**Fig. 3** Selectivity towards (**A**) oxygenated compounds, (**B**) hydrocarbons and (**C**) C-atoms per molecule of hydrocarbon in biooils from PS pyrolysis catalyzed by Ni-zeolites

### 3.3 Biooil upgrade

The effects of the Ni modified zeolites on the product distribution of PS pyrolysis are presented in Fig. 3. Compounds found in the biooil were classified into oxygenated compounds (acids, aldehydes, ketones, phenols, alcohols, furans and esters) and hydrocarbons (aliphatics and aromatics). As can be observed, $O_2$-containing compounds were the main products in the thermal pyrolysis of PS. As expected, when Ni-zeolites were employed, $O_2$-containing compounds decreased while hydrocarbons selectivity increased. Considering the reactor disposal, once the pyrolysis occurred, the vapors came in contact with the solid catalyst. Active sites are present on the surface and in the pores of the zeolites. When pyrolysis products contact them, reactions such as cracking, isomerization, aromatization and polymerization occurred. Thus, selectivity towards hydrocarbons increased. The main compounds identified were similar to those reported in literature [6] and they are listed in Table S1**,** in the Supporting Information file.

Biooils from all catalyzed reactions presented higher concentration of hydrocarbons than the thermal run. Ni (1) Z and Ni (8) Z catalysts presented lower hydrocarbons selectivity than the parent HZ zeolite. It was noticeable the reduction on hydrocarbons selectivity in Ni (8) Z catalyzed reactions. As previously described, the presence of large oxide particles blocked the pores of the zeolite making the internal acid sites inaccessible. As consequence, lower hydrocarbons selectivity was obtained.

Ni (5) Z showed considerable deoxygenation and the highest hydrocarbons selectivity. This result can be explained partly by the physicochemical and textural characteristics of the zeolites employed and partly by the presence of the metal particles. As previously discussed, Ni (5) Z presented the highest amount of LAS and BAS, suggesting that there would be an optimal amount of metal to incorporate on a determined zeolite matrix. Kostyniuk et al. [19] found that zeolites with 5 wt% of Ni were the most active catalysts in hydrogenation, hydrocracking and isomerization reactions of biomass tar model compound mixture. On the other hand, it has been proposed that the impregnation of the catalyst with nickel significantly improved the selectivity towards hydrocarbons in the biooil from pyrolysis of lignocellulosic biomass [27]. In this sense, the nickel particles strongly promote the hydrogen-transfer reactions that favor the formation of hydrocarbons during the catalytic improvement of the pyrolysis vapors [28].

It should be noted that the hydrocarbon fraction was mainly composed by aromatics (Fig. 3B). It is well known that aromatization reactions require synergies of Brønsted and Lewis acid sites. Although BAS are active sites for aromatization reactions, dehydrogenation or

hydrogen atom transfer reaction occurs on the LAS [29]. As presented in Table 1, Ni (5) Z zeolite had the highest LAS and BAS. Consequently, the lowest oxygenated compounds and highest aromatic selectivities were obtained over this material.

Figure 3C shows hydrocarbons distribution in the liquid products, according to the number of C-atoms per molecule. As can be observed, selectivity towards C10–C15 compounds was extremely low in the studied reactions.

On the contrary, Ni (5) Z favored the cracking to yield higher amounts of low molecular weight compounds, with 7–9 carbon atoms per molecule. This group includes valuable products like xylenes (C8), cumene and trimethylbenzene (TMB, C9). Less valuable toluene (C7) was also present in the analyzed biooil. Nevertheless, the petrochemical industry can convert toluene to those important products by aromatic hydrocarbons transformations reactions. Xylene, a high demand compound in the chemical market, could also be produced through catalytic transalkylation of toluene with TMB [30].

Among $O_2$-containing compounds, two interesting compounds for the fine chemical industry were observed: furfural and 5-HMF. The former is mainly used as a selective solvent for the refining of lubricating oils and diesel fuels and as an intermediate chemical in the manufacturing of many solvents, plastics and agrochemicals. The latter can be converted to a variety of value-added furan compounds and can be used for the synthesis of polymers as it contains similar structure as aromatics. Synthesis of 5-HMF from biomass molecules, involves hydrolysis of the polymeric carbohydrates, isomerization of glucose into fructose and finally dehydration to 5-HMF [31].

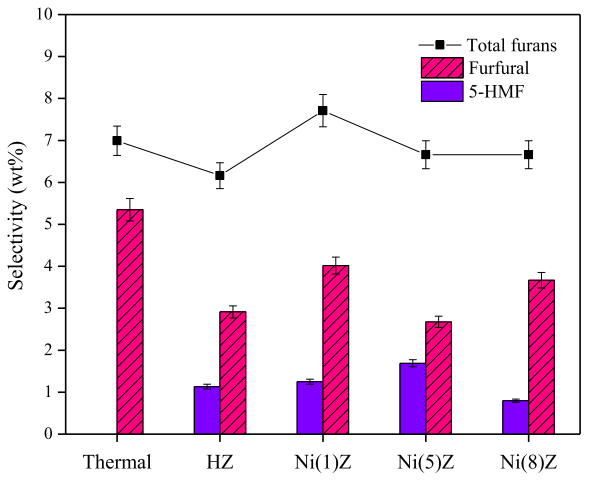


**Fig. 4** Selectivity towards furans, furfural and 5-HMF in biooils from PS pyrolysis catalyzed by Ni-zeolites

Figure 4 shows the selectivity towards furans, furfural and 5-HMF. From the figure it is evident that 5-HMF was promoted by all catalysts since a complete absence of this compound was observed in the thermal reaction. Approximately 50% of furans corresponded to furfural and 5-HMF. Similarly to hydrocarbons, Ni (5) Z was the most active catalyst in favoring the formation of 5-HMF. In the chemical pathway for cellulose transformation to 5-HMF, Brønsted acidity is believed to promote the depolymerization of oligosaccharides to monomeric anhydro-sugars [32]. The isomerization to fructose seems to occur in the presence of LAS and the dehydration is thought to be promoted by BAS [33].

### 3.4 Catalyst deactivation

Coke nature of spent catalysts was studied by FTIR spectroscopy (Fig. 5A). An intense band at 3434 $cm^{-1}$ could be observed in all samples. That band is attributed to bridging hydroxyl groups, while the smaller band at 3234 $cm^{-1}$ is attributed to H-bonding between acidic hydroxyl groups and adsorbed molecules. The bands between 2800 and 3000 $cm^{-1}$ are attributed to the CH stretching modes (symmetric and asymmetric) of $CH_3$ groups. The bands from 1300 to 1700 $cm^{-1}$ can be assigned to the CH bending of paraffinic groups and the CC stretching modes of unsaturated groups. The bands around 1450–1700 $cm^{-1}$ are mainly attributed to aromatics structure vibration [34]. Figure 5B shows FTIR spectroscopy of fresh HZ where a total absence of carbon signals was observed.

Catalyst stability was evaluated with six consecutive reaction cycles. Since products yields (biooil, biochar and gases) did not suffer significant variations, six main compounds, including furans and aromatics, were chosen to test the zeolite deactivation. The most active catalyst, Ni (5) Z, was selected and its re-uses are presented in Fig. 6. Results showed partially deactivation just in the second cycle. This behavior can be explained by coke deposition. From Table 1, it could be observed how $S_{BET}$ decreased in all spent catalysts. In the case of Ni (5) Z, an area loss of about 100 $m^2\ g^{-1}$ was obtained after the first use.

From Fig. 6 it is possible to confirm an increment on furfural selectivity as reuses cycles advanced. However, the other compounds analyzed were reduced (selectivities < 1 wt%). This behavior could be explained by the surface area reduction as previously commented. When zeolites pores were physically blocked by coke deposition, pyrolysis products could not get in contact with the catalyst active sites. Thus, reaction products were quite similar to non-catalytic reactions. Besides, Renzini et al. [20] found that coke deposition over ZMS-11 zeolites caused a decrease of both BAS and LAS. This significant reduction on active sites is the reason of the

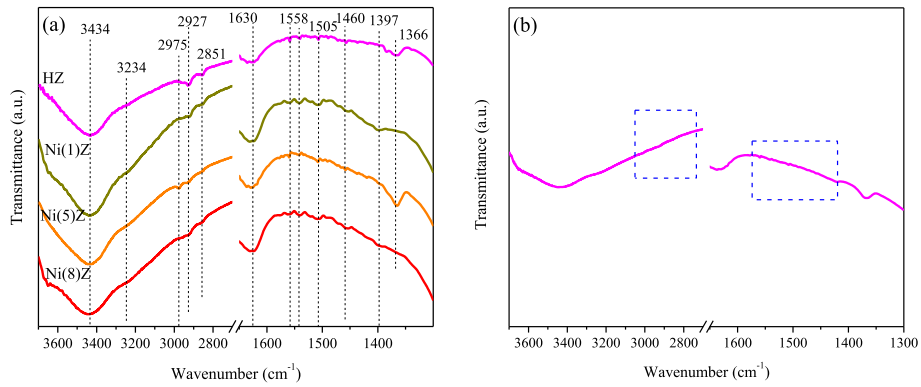


**Fig. 5** FTIR spectra of (**A**) spent catalysts and (**B**) fresh HZ catalyst. Dash squares emphasize lack of carbon signals

selectivity loss in the selected compounds (toluene, cumene, TMB, xylene and 5-HMF). The furfural was present in the biooil in higher proportions.

However, it is noteworthy that upon deactivation Ni (5) Z could be easily regenerated by calcination. After that, catalytic activity was completely recovered. Figure S1 presents XRD pattern of the regenerated catalyst, confirming ZSM-11 structure and crystallinity. Coke deposition resulted in a temporarily catalyst poisoning and acid sites blockage that could be thermally solved.

### 3.5 Activated biochar characterization

Table 3 presents physicochemical characteristics of the synthetized AB samples. Biochar is presented for comparison reasons. As can be observed, $S_{BET}$ doubled when the KOH:biochar ratio increased from 1:1 to 3:1. In general, BET surface area increases when KOH content or temperature increase [13, 35].

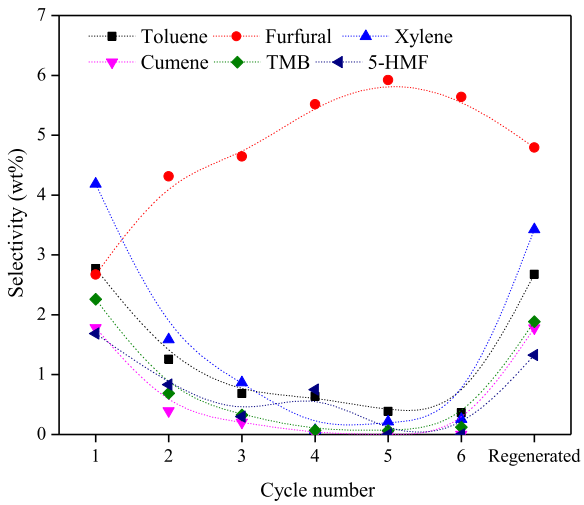


**Fig. 6** Compounds selectivity in consecutive cycles of PS pyrolysis over Ni(5) Z

Proximate analysis revealed that fixed carbon in the activated biochars was higher than in the starting biomass, resulting from an effective carbonization process [36]. As the temperature increases, it is expected that the carbon content increases and that of the volatiles decreases, since devolatilization processes predominantly occur [37]. From the analysis of activated materials, it could be observed that the fixed carbon content decreased as the surface area increased, thus registering AB 3:1 sample the lowest fixed carbon value. Moisture content in this sample was almost 4 wt% higher, suggesting that it is slightly more hygroscopic than AB 1:1.

XRD diffractograms and Raman spectra display the crystallographic structures of the activated materials (Fig. 7). All specimens presented a broad band located at $2\theta = 20–30°$ which is characteristic of amorphous materials, suggesting the existence of amorphous carbon caused by incomplete carbonization [38]. The peak at $2\theta = 23.5°$ corresponds to the (002) graphite planes. From Fig. 7A it can be observed that this broad peak is stronger in biochar and weaker in the AB samples, proving an increase in the degree of graphitization. Figure 7B presents Raman spectra of the as-prepared porous carbon materials. The D-bands (~ 1356 $cm^{-1}$) and G-bands (~ 1604 $cm^{-1}$) correspond to the disordered carbon and graphite carbon, respectively [39]. D and G bands ratio ($I_D/I_G$) changed from 0.96 in pyrolysis biochar to 1.00 in AB 3:1 sample, indicating a higher graphitization degree at a higher temperature.

**Table 3** Physicochemical characteristics of activated biochars

| | Proximate analysis (wt%)[a] | | | | $S_{BET}$ |
|---|---|---|---|---|---|
| | Moisture | Volatile matter | Fix carbon | Ash | ($m^2\ g^{-1}$) |
| Biochar | 6.8 | 28.0 | 58.7 | 6.5 | 215 |
| AB 1:1 | 20.1 | 11.0 | 64.5 | 4.5 | 832 |
| AB 3:1 | 23.9 | 12.6 | 58.5 | 5.0 | 1645 |

[a] Determined by TGA

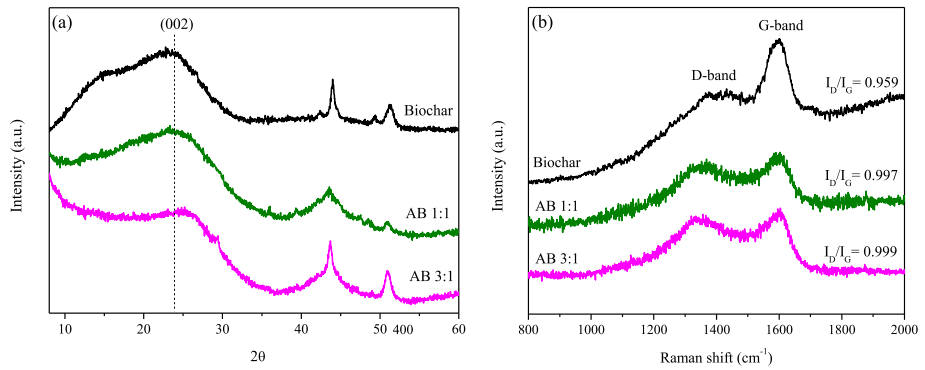


**Fig. 7** (**A**) XRD patterns and (**B**) Raman spectra of activated biochars

The FTIR spectra of the AB samples are shown in Fig. 8. The presence of surface functional groups is considered an important factor that determines the adsorption behavior of activated carbons. The vibrations of some functional groups could be observed. The band at 400–750 $cm^{-1}$ was assigned to the stretching vibration of C-C and the one at 750–900 $cm^{-1}$ was responsible for the bending of C-H. The signals at 1050 and 1250 $cm^{-1}$ were attributed to the vibrations of C-O and C-O-C and the peak at 1480 $cm^{-1}$ would indicate the stretching vibration C=C [35]. The signal at ~ 1600 $cm^{-1}$ can be attributed to C=C stretching (aromatic components) and C=O stretching of conjugated ketones. The signal at 1700 $cm^{-1}$ was assigned to the C=O stretch and the one at 1750 $cm^{-1}$ resulted from the presence of -COOH groups. While the band at 2800–2900 $cm^{-1}$ was responsible for the stretching of aliphatic CH, the broad band at 3400 $cm^{-1}$ was assigned to the vibration of –OH, corresponding to adsorbed water molecules [35, 40].

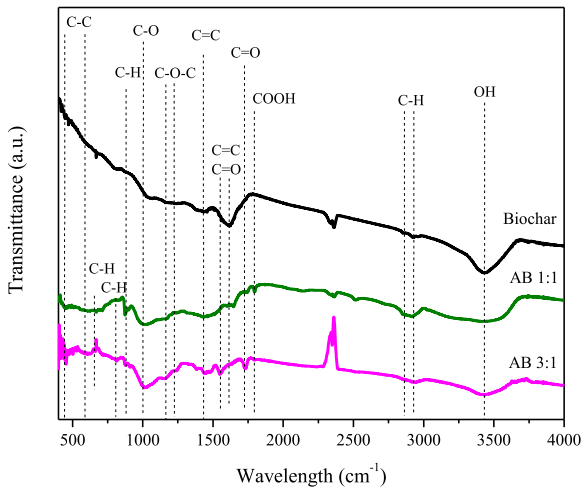


**Fig. 8** FTIR spectra of activated biochars

SEM micrographs of the as-prepared materials are presented in Fig. 9. AB 1:1 sample presented a rib-like structure (Fig. 9A) on which the presence of numerous dispersed pores could be observed. As the KOH content increased, the precursor (biochar) continued decomposing, and the formation of many new macropores could be observed in AB 3:1 sample (Fig. 9B). Thus it indicated that the ribs observed in AB 1:1 were transformed into channels in AB 3:1. Consequently, the opening of the macropores possibly contributed to the formation of new micro and mesopores on the internal surfaces.

## 4 Conclusions

With the aim of promoting the circular bioeconomy, the recycling of PS in two subsequent product systems was studied. The first system consisted of catalytic fast pyrolysis of the residual biomass where a group of Ni-ZSM-11 matrices was tested. When varying Ni content, a surface area reduction was obtained, but acid sites were improved. From the evaluated materials, Ni (5) Z showed the best results in terms of hydrocarbons and platform molecules selectivities. This catalyst was further measured in terms of stability over several reaction cycles. The temporary poisoning was easily solved by calcination, after which the material recovered its pristine crystallinity and catalytic behavior. Thus, it is possible to affirm that nickel ZSM-11 zeolites with a 5 wt% of loading are ideal catalysts for the pyrolytic conversion of PS to interesting platform molecules.

The second system consisted of synthetizing AB employing the residual biochar from the previous pyrolysis as the precursor. The materials were produced by a simple thermo-chemical procedure, employing KOH as activation agent. Specific surface area could be significantly increased upon activation, from 215 $m^2\ g^{-1}$ in biochar to 1645 $m^2\ g^{-1}$ when KOH:biochar ratio was 3:1. Considering the type and quantity of surface functional groups found on these materials, they could be used for a variety of sorption processes.

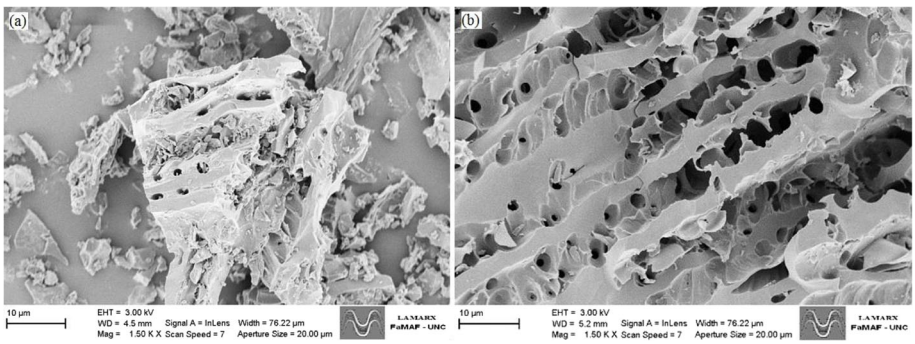


**Fig. 9** SEM micrographs of activated biochars. (**A**) AB 1:1, (**B**) AB 3:1

These results proved to be an example of an efficient biobased renewable resource management achieving near-zero-waste conditions. Resources were recovered and transformed by simple thermochemical methods.

## 5 Supplementary Information

The online version contains supplementary material available at https://doi.org/10.1186/s42834-021-00112-9.

**Additional file 1.**

### Acknowledgements

The authors of this work would like to thank Universidad Tecnológica Nacional (PID UTN 6562), Ministerio de Ciencia y Tecnología de Córdoba (PIOdo18) and Consejo Nacional de Investigaciones Científicas y Técnicas (CONICET).

### Authors' contributions

Carla S. Fermanelli: investigation, methodology, data curation, writing – original draft. Adrián Chiappori: resources. Liliana Pierella: project administration. Clara Saux: conceptualization, writing – review and editing, supervision. All authors have given approval to the final version of the manuscript.

### Funding

Not applicable.

### Availability of data and materials

All data generated or analyzed during this study are available from the corresponding author, upon reasonable request. The necessary data that were generated and analyzed during the study are included in this published article.

## Declarations

### Competing interests

The authors declare they have no competing interest.

### Author details

[1]Phytophalogy and Agricultural Modeling Unit, National Institute of Agricultural Technology, 5020 Cordoba, Argentina. [2]Chemical Research and Technology Center, National Technological University, 5016 Cordoba, Argentina. [3]Acoustics Research and Transfer Center, National Technological University, 5016 Cordoba, Argentina.

Received: 16 June 2021 Accepted: 2 December 2021
Published online: 08 January 2022

### References

1. Kapoor R, Ghosh P, Kumar M, Sengupta S, Gupta A, Kumar SS, et al. Valorization of agricultural waste for biogas based circular economy in India: a research outlook. Bioresour Technol. 2020;304:123036.
2. Kershaw EH, Hartley S, McLeod C, Polson P. The sustainable path to a circular bioeconomy. Trends Biotechnol. 2021;39:542–5.
3. FAO. FAOSTAT 2021: Crops and Livestock Products. Rome: Food and Agriculture Organization; 2021. http://www.fao.org/faostat/en/?#data/QCL.
4. Fermanelli CS, Galarza ED, Pierella LB, Renzini MS, Saux C. How to valorize peanut shells by a simple thermal-catalytic method. Top Catal. 2019;62:918–30.
5. Fermanelli CS, Cordoba A, Pierella LB, Saux C. Pyrolysis and copyrolysis of three lignocellulosic biomass residues from the agro-food industry: a comparative study. Waste Manage. 2020;102:362–70.
6. Dai LL, Wang YP, Liu YH, Ruan R, Duan DL, Zhao YF, et al. Catalytic fast pyrolysis of torrefied corn cob to aromatic hydrocarbons over Ni-modified hierarchical ZSM-5 catalyst. Bioresour Technol. 2019;272:407–14.
7. Kan T, Strezov V, Evans T, He J, Kumar R, Lu Q. Catalytic pyrolysis of lignocellulosic biomass: a review of variations in process factors and system structure. Renew Sust Energ Rev. 2020;134:110305.
8. Olofsson J, Borjesson P. Residual biomass as resource – life-cycle environmental impact of wastes in circular resource systems. J Clean Prod. 2018;196:997–1006.
9. Sakhiya AK, Baghel P, Anand A, Vijay VK, Kaushal P. A comparative study of physical and chemical activation of rice straw derived biochar to enhance $Zn^{+2}$ adsorption. Bioresour Technol Rep. 2021;15:100774.
10. Galarza ED, Fermanelli CS, Pierella LB, Saux C, Renzini MS. Influence of the Sn incorporation method in ZSM-11 zeolites in the distribution of bio-oil products obtained from biomass pyrolysis. J Anal Appl Pyrol. 2021;156:105116.
11. Emeis CA. Determination of integrated molar extinction coefficients for infrared absorption bands of pyridine adsorbed on solid acid catalysts. J Catal. 1993;141:347–54.
12. Aho A, Kumar N, Eranen K, Salmi T, Hupa M, Murzin DY. Catalytic pyrolysis of woody biomass in a fluidized bed reactor: influence of the zeolite structure. Fuel. 2008;87:2493–501.
13. Fu YH, Shen YF, Zhang ZD, Ge XL, Chen MD. Activated bio-chars derived from rice husk via one- and two-step KOH-catalyzed pyrolysis for phenol adsorption. Sci Total Environ. 2019;646:1567–77.
14. Saldarriaga JF, Aguado R, Pablos A, Amutio M, Olazar M, Bilbao J. Fast characterization of biomass fuels by thermogravimetric analysis (TGA). Fuel. 2015;140:744–51.
15. Iliopoulou EF, Stefanidis SD, Kalogiannis KG, Delimitis A, Lappas AA, Triantafyllidis KS. Catalytic upgrading of biomass pyrolysis vapors using transition metal-modified ZSM-5 zeolite. Appl Catal B-Environ. 2012;127:281–90.
16. Brodu N, Manero MH, Andriantsiferana C, Pic JS, Valdes H. Role of Lewis acid sites of ZSM-5 zeolite on gaseous ozone abatement. Chem Eng J. 2013;231:281–6.

17. Li L, Stroobants C, Lin KF, Jacobs PA, Sels BF, Pescarmona PP. Selective conversion of trioses to lactates over Lewis acid heterogeneous catalysts. Green Chem. 2011;13:1175–81.
18. Kostyniuk A, Key D, Mdleleni M. 1-hexene isomerization over bimetallic M-Mo-ZSM-5 (M: Fe, Co, Ni) zeolite catalysts: effects of transition metals addition on the catalytic performance. J Energy Inst. 2020;93:552–64.
19. Kostyniuk A, Bajec D, Likozar B. Catalytic hydrogenation, hydrocracking and isomerization reactions of biomass tar model compound mixture over Ni-modified zeolite catalysts in packed bed reactor. Renew Energ. 2021;167: 409–24.
20. Renzini MS, Lerici LC, Sedran U, Pierella LB. Stability of ZSM-11 and BETA zeolites during the catalytic cracking of low-density polyethylene. J Anal Appl Pyrol. 2011;92:450–5.
21. Hu ZP, Weng CC, Chen C, Yuan ZY. Catalytic decomposition of ammonia to COx-free hydrogen over Ni/ZSM-5 catalysts: a comparative study of the preparation methods. Appl Catal A-Gen. 2018;562:49–57.
22. Zanjanchi MA, Razavi A. Identification and estimation of extra-framework aluminium in acidic mazzite by diffuse reflectance spectroscopy. Spectrochim Acta A. 2001;57:119–27.
23. Li XM, Han DZ, Wang H, Liu GB, Wang B, Li Z, et al. Propene oligomerization to high-quality liquid fuels over Ni/HZSM-5. Fuel. 2015;144:9–14.
24. Graca I, Gonzalez LV, Bacariza MC, Fernandes A, Henriques C, Lopes JM, et al. $CO_2$ hydrogenation into $CH_4$ on NiHNaUSY zeolites. Appl Catal B-Environ. 2014;147:101–10.
25. Stanton AR, Iisa K, Yung MM, Magrini KA. Catalytic fast pyrolysis with metal-modified ZSM-5 catalysts in inert and hydrogen atmospheres. J Anal Appl Pyrol. 2018;135:199–208.
26. Rezaei PS, Shafaghat H, Daud WMAW. Production of green aromatics and olefins by catalytic cracking of oxygenate compounds derived from biomass pyrolysis: a review. Appl Catal A-Gen. 2014;469:490–511.
27. Veses A, Puertolas B, Callen MS, Garcia T. Catalytic upgrading of biomass derived pyrolysis vapors over metal-loaded ZSM-5 zeolites: effect of different metal cations on the bio-oil final properties. Micropor Mesopor Mat. 2015;209:189–96.
28. Botas JA, Serrano DP, Garcia A, de Vicente J, Ramos R. Catalytic conversion of rapeseed oil into raw chemicals and fuels over Ni- and Mo-modified nanocrystalline ZSM-5 zeolite. Catal Today. 2012;195:59–70.
29. Cai YX, Fan YS, Li XH, Chen L, Wang JJ. Preparation of refined bio-oil by catalytic transformation of vapors derived from vacuum pyrolysis of rape straw over modified HZSM-5. Energy. 2016;102:95–105.
30. Almulla FM, Ali SA, Aldossary MR, Alnaimi EI, Jumah AB, Garforth AA. Transalkylation of 1,2,4-trimethylbenzene with toluene over large pore zeolites: role of pore structure and acidity. Appl Catal A-Gen. 2020;608: 117886.
31. Yu IKM, Tsang DCW, Yip ACK, Chen SS, Ok YS, Poon CS. Valorization of food waste into hydroxymethylfurfural: dual role of metal ions in successive conversion steps. Bioresour Technol. 2016;219:338–47.
32. Zhang HY, Liu XJ, Lu MZ, Hu XY, Lu LG, Tian XN, et al. Role of Brønsted acid in selective production of furfural in biomass pyrolysis. Bioresour Technol. 2014;169:800–3.
33. Marianou AA, Michailof CM, Pineda A, Iliopoulou EF, Triantafyllidis KS, Lappas AA. Effect of Lewis and Brønsted acidity on glucose conversion to 5-HMF and lactic acid in aqueous and organic media. Appl Catal A-Gen. 2018; 555:75–87.
34. Chaouati N, Soualah A, Chater M, Tarighi M, Pinard L. Mechanisms of coke growth on mordenite zeolite. J Catal. 2016;344:354–64.
35. Shen YF, Zhou YW, Fu YH, Zhang NY. Activated carbons synthesized from unaltered and pelletized biomass wastes for bio-tar adsorption in different phases. Renew Energ. 2020;146:1700–9.
36. Ratan JK, Kaur M, Adiraju B. Synthesis of activated carbon from agricultural waste using a simple method: characterization, parametric and isotherms study. Mater Today Proc. 2018;5:3334–45.
37. Rashidi NA, Yusup S, Ahmad MM, Mohamed NM, Hameed BH. Activated carbon from the renewable agricultural residues using single step physical activation: a preliminary analysis. APCBEE Procedia. 2012;3:84–92.
38. Lin H, Liu Y, Chang Z, Yan S, Liu S, Han S. A new method of synthesizing hemicellulose-derived porous activated carbon for high-performance supercapacitors. Micropor Mesopor Mat. 2020;292:109707.
39. Guo CZ, Hu R, Liao WL, Li ZB, Sun LT, Shi DP, et al. Protein-enriched fish "biowaste" converted to three-dimensional porous carbon nano-network for advanced oxygen reduction electrocatalysis. Electrochim Acta. 2017;236: 228–38.
40. Lee J, Yang X, Cho SH, Kim JK, Lee SS, Tsang DCW, et al. Pyrolysis process of agricultural waste using $CO_2$ for waste management, energy recovery, and biochar fabrication. Appl Energ. 2017;185:214–22.

## Publisher's Note